Journal of Alloys and Compounds 509 (2011) 3726–3734

Contents lists available at ScienceDirect

Journal of Alloys and Compounds

journal homepage: www.elsevier.com/locate/jallcom

# Deformation induced thermoremanent magnetisation in an FeMnNiCr antiferromagnetic alloy

D. Geissler[a,b], K.-H. Müller[a], J. Freudenberger[a,*], K. Nenkov[a], M. Krautz[a,b], J. Eickemeyer[a], L. Schultz[a,b]

[a] IFW Dresden, P.O. Box 270116, 01171 Dresden, Germany
[b] TU Dresden, Institute of Materials Science, 01062 Dresden, Germany

ARTICLE INFO

*Article history:*
Received 31 August 2010
Received in revised form
21 December 2010
Accepted 22 December 2010
Available online 29 December 2010

*Keywords:*
Antiferromagnet
Magnetic properties
Plastic deformation
Superparamagnetism
Exchange anisotropy

ABSTRACT

In an austenitic $Fe_{61.5}Mn_{23}Ni_7Cr_{8.5}$ antiferromagnetic (afm) alloy deformation results in a splitting between magnetisation-vs.-temperature curves measured during field cooling (FC) below the Néel temperature and those measured at the same field after zero-field cooling (ZFC). Furthermore, a thermoremanent magnetisation (TRM) appears that corresponds to the splitting between zero-field and field cooled thermomagnetic measurements for a given cooling field and scales with the degree of deformation. This TRM is attributed to the deformation induced defects which act as a source of uncompensated magnetic moments and interact with the bulk afm moments. This interpretation is also supported by the fact that the net magnetic moments vanish above the Néel temperature. The TRM does not saturate in fields of up to 7 T, applied during cooling, and cannot be switched by fields up to 7 T. Within the investigated field range of −7 T to 7 T the magnetisation-vs.-field curves show a stable shift along the magnetisation axis. Thus, the uncompensated moments appear to be strongly exchange coupled to the afm matrix surrounding them. Within the series of experiments the maximum TRM reached after FC in 7 T corresponds to about $4 \times 10^{-4} \mu_B$/atom (Bohr magneton) of the maximum deformed afm sample. The Néel temperature decreases due to deformation.



## 1. Introduction

The influence of internal defects on the magnetic properties of metallic alloy antiferromagnets is a rarely investigated subject. With respect to the composition of the alloy $Fe_{61.5}Mn_{23}Ni_7Cr_{8.5}$ (at.%) investigated here, there is clear correlation to the antiferromagnetism of FeMn- and FeMn-base alloys. Structurally the addition of Mn to Fe results in an extension of the austenite, face centred cubic (fcc) γ-phase to lower temperatures. Effectively, above 27.3 at.% Mn there is no transformation of austenite upon cooling anymore [1]. The addition of Ni results in a further stabilisation of the metastable austenite phase at and below room temperature with respect to transformation into martensitic phases. The ternary phase diagram of Fe–Mn–Ni shows a broad composition field of austenite ranging from antiferromagnetism on the FeMn-side over a valley with spin-glass-like and reentrant spin glass magnetic phenomena to ferromagnetism in the Ni-rich corner [2,3]. Alloying with Cr improves the corrosion resistance. Up to about 12 at.% Cr, its addition to the austenitic FeMn-phase has no structural and only negligible influence on the antiferromagnetic properties [4]. Therefore, the annealed state of the investigated alloy can be addressed as austenitic and antiferromagnetic (afm).

The afm properties of the austenitic FeMn-system have been intensively studied in the past, e.g. [5,6]. It is generally accepted, that the afm spin structure in the composition range from about 20 to 60 at.% Mn is a non-collinear spin configuration with the atomic magnetic moments pointing along the four ⟨1 1 1⟩-axis of the fcc structure, thus compensating the magnetic moment within the afm order [5–8]. The same spin structure was discussed by Kouvel and Kasper [9] for the disordered afm Fe–Mn–Ni-alloys.

Antiferromagnetic FeMn-alloys, which are random solid solutions, show nearly constant susceptibility with rising temperature in the paramagnetic state. This is accounted for Pauli paramagnetism, i.e. for an itinerant electron based magnetism in these alloys [6,10]. By alloying Ni into γ-FeMn the susceptibility decreases not only below but also above the Néel temperature, $T_N$, which was interpreted as localisation of moments at the Ni sites [10].

The austenitic phase is practically stable and the fcc structure is maintained to liquid helium temperature in the Fe–Mn–Ni-system, if the Fe-content is below 65% for any Ni–Mn-ratio [3]. By considering the influence of moderate Cr-additions on to the fcc Fe–Mn alloys this should also hold for the present alloy. Nevertheless, the austenite is thermodynamically metastable. A consequence of this metastability is structural instability during plastic deformation which is usually referred to in terms of the stacking fault energy, γ

* Corresponding author.
*E-mail address:* j.freudenberger@ifw-dresden.de (J. Freudenberger).

0925-8388/$ – see front matter © 2011 Elsevier B.V. All rights reserved.
doi:10.1016/j.jallcom.2010.12.158

(SFE). In the composition range of the investigated alloy this instability causes twinning induced plasticity (TWIP) [11–14] in addition to 'conventional' slip deformation [15], a process that influences the microstructure but preserves the austenite phase. At lower SFE, i.e. lower Mn concentrations, this instability causes $\varepsilon$-martensite formation by transformation induced plasticity (TRIP [11,12]).

Since in an afm spin structure the moments carried by the lattice sites are compensated to zero net magnetic moment by a strict arrangement of sublattices with differently oriented spins, the afm spin structure is sensitive to any kind of disorder in the lattice structure. Deformation of a metallic alloy gives rise to different types of disorder, in particular lattice defects of different dimensionality, that have to be considered with respect to the antiferromagnetic state. These are predominantly dislocations due to slip deformation and small angle grain boundaries (SAGB) or even high angle grain boundaries (HAGB) as a consequence of rising degree of deformation and dislocation density. Deformation twinning (TWIP) is also considered to result from dislocation reactions [15,16].

As a first effect of these defects, clusters of uncompensated magnetic moments occur due to the disturbance of the afm spin lattice order. Uncompensated moments resulting from imperfect compensation of afm sublattices have been first described by Néel [17]. In small afm particles uncompensated moments are likely to appear due to the termination at the particle surface, because, with respect to the small dimensions, a fully compensated moment is most probably not consistent with the afm spin order.

A further effect of disorder in antiferromagnets is local weakening of afm exchange interaction and possibly even local changes of its sign. Moreover, in antiferromagnets with localised staggered magnetic moments disorder causes frustration [18], meaning that all two-spin interactions cannot simultaneously exist in their lowest energy configuration. Randomness combined with frustration typically results in spin-glass-like behaviour [19]. Certain types of frustration also occur in itinerant antiferromagnets [20].

The uncompensated surface moments of afm nanoparticles can either be frustrated resulting in spin-glass-like behaviour or they strongly interact with the parent antiferromagnet. In the latter case, the uncompensated moments should add up to a spontaneous magnetic moment of the particle below the Néel temperature, $T_N$ [17,21]. If a system of afm nanoparticles is cooled in a magnetic field from a temperature above $T_N$ to below $T_N$ the field will orient the uncompensated moments and, due to their coupling to the antiferromagnetic particle volume, the alignment of the spins in the afm sublattices will be governed by the field. If then the field is switched off, a thermoremanent magnetisation (TRM) will occur as reported, e.g. in [22]. This was interpreted as a case of exchange anisotropy [23,24] where a 'ferromagnetic' entity is coupled to an antiferromagnet. Exchange anisotropy is a unidirectional anisotropy resulting in a shift of the hysteresis loop of the formerly non-exchange coupled ferromagnetic entity on the field axis [24].

A quite similar situation is given in disordered, structurally single phase materials, that might allow for short range order, with intrinsically coexisting or competing ferro- and antiferromagnetic exchange interactions. In such systems related phenomena have been observed in the context of mictomagnetism and are nowadays mostly referred to as spin glass or cluster glass behaviour. Kouvel et al. [25–27] reported exchange anisotropy for the (Fe)NiMn-system at compositions that are located in the spin glass valley that divides the afm region of the austenite phase on the Fe- and Mn-rich side from the ferromagnetic (fm) austenitic Ni-rich side (in the ternary Fe–Mn–Ni phase diagram [2,4]).

For the disordered $Ni_3Mn$-alloy Goldfarb and Patton [28] reported TRM that according to their interpretation represents superparamagnetic (spp) clusters with predominantly ferromagnetic order that block and exchange couple during field cooling to a viscous and subsequently frozen glassy environment with dominating afm order. Due to the existence of the fm ordered phases in the Ni–Mn-system they believe that the spp clusters were already formed by short range ordering during quenching.

Alloying more Fe or Mn in the disordered alloys with respect to the $Ni_3Mn$-composition, leads to a gradual transition from cluster glass towards pure antiferromagnetism as reported in [9,26,27] and discussed above. Therefore the exchange anisotropy of field cooled states is also increasing [26,27].

In recent years a growing interest in uncompensated magnetic moments within afm materials has evolved as they influence the contribution of the afm part of exchange bias (EB) systems [29–32] which are also set by field cooling procedures [33].

## 2. Experimental

The alloy was molten from pure elements (grade 2N or higher) in a BALZERS induction furnace under vacuum and argon during the last step at which Mn was charged. The melt was then cast to a cylindrically shaped ingot of 35 mm in diameter (length ≈200 mm). The nominal composition of Fe–24Mn–7Ni–8Cr (mass%) was checked by wet-chemical analysis of the fully processed material by ICP-OES (Inductively Coupled Plasma Optical Emission Spectrometry) and revealed an effective composition of $Fe_{61.5}Mn_{23}Ni_7Cr_{8.5}$ (at.%, with a relative standard deviation of <0.2%). Impurities are mostly sulfur and selenium, chemically bonded in the form of Mn(S, Se) as determined semi-quantitatively by energy dispersive X-ray spectroscopy (not shown here).

Following casting, the ingot was hot forged at 1000 °C in air to rods of 16 mm in diameter in semi-circular die blocks. After an intermediate forging step a homogenisation heat treatment at 1025 °C/20 h was applied in air utilising a sealed KNU-foil in order to prevent severe oxidation. Cooling was done by water quenching.

The alloy was subsequently machined to remove the oxide layer and cold drawn to a wire of 6 mm in diameter. Then the alloy was annealed under the same conditions as before but at 1100 °C and for 20 min only. This treatment marks the starting point for cold deformation which was performed following two different routes. In the first case cold wire drawing in several steps was applied to achieve a diameter of 0.9 mm. Samples of rising degree of deformation were taken during this process. The round wire was finally cold rolled to a thickness of 0.3 mm, which resulted in a logarithmic degree of deformation of $\eta = \ln(A_0/A) = 4.01$. $A_0$ is the cross section of the annealed state and $A$ the cross section of the respective deformed state.

In the second route cold deformed samples for the lowest degrees of deformation were obtained by tensile testing. As a measure for the impact of increasing deformation Vickers indentation was used to characterise the hardening evolution over the whole range. The applied load on metallographically polished samples was 200 p (Pond: 200 p = 1.962 N) at a dwell time of 10 s (HV 0.2–10).

X-ray powder diffraction studies on filings of annealed and deformed samples were used for phase analysis. The development of the microstructure caused by cold deformation is not accessible by means of line profile analysis because either the deformed state will be strongly modified during XRD sample preparation (filing) or the textured bulk condition would not provide a sound X-ray pattern for line profile analysis. Also the detection of microstructural features, such as dislocations and stacking faults of the deformed state by transition electron microscopy (TEM) is unpromising because the observed effects are connected to degrees of deformation, where lattice strains dominate TEM-imaging contrast. Furthermore by observation of single dislocations there would be no direct link to the magnetic effects observed.

The deformation specific changes in the microstructure of the alloy can be appropriately represented by the electron backscatter diffraction (EBSD) method. At moderate degree of deformation it allows to directly identify deformation twins, which of course would also be possible by TEM. Furthermore, intra-grain misorientation as determined by EBSD orientation imaging microscopy gives a qualitative measure of plasticity due to dislocation slip, because it is the result of the whole dislocation ensemble and, therefore, the dislocation density. Microstructural investigations as exemplarily presented in Fig. 5 were done on metallographically polished sections of deformed samples. Details are given in the figure caption.

Samples for magnetisation measurements were cut to small pieces and ground while cooling in order to avoid surface oxidation effects.

Temperature and field dependent magnetisation measurements were accomplished after zero-field cooling (ZFC) and during as well as after field cooling (FC) from above the Néel temperature utilising either a Quantum Design MPMS Superconducting Quantum Interference Device (SQUID) magnetometer or a Quantum Design PPMS equipped with a vibrating sample magnetometer (VSM) as indicated in the corresponding figures. Cooling fields and measuring fields were applied parallel to the direction of magnetisation measurement. The measured magnetic moments of the samples are plotted by means of the (specific) magnetisation $\sigma$ ($[\sigma] = Am^2/kg$).

Different states of thermoremanent magnetisation [34], $TRM(H_{FC})$, were set by cooling from above the Néel temperature, $T_N$, to a given temperature in a defined cooling field, $H_{FC}$, which is switched off after the cooling procedure. Results of subsequent measurements of magnetisation in dependence on temperature will be designated $TRM(T)$ where warming and cooling will be indicated by arrows because

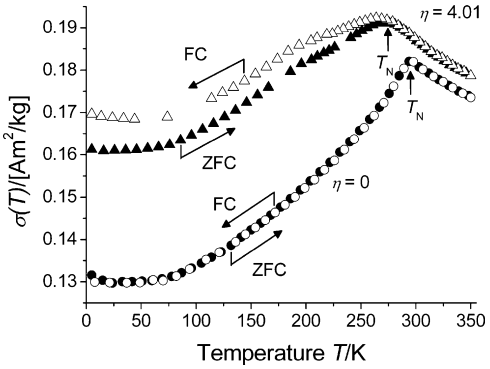


**Fig. 1.** Magnetisation-vs.-temperature curves of samples with different logarithmic degree of deformation $\eta$, measured in a SQUID at 1$T$ applied field: filled symbols – after zero-field cooling (ZFC); open symbols – *during* field cooling (FC at 1 T); circles – annealed state, $\eta = 0$ (no splitting between ZFC an FC); triangles – maximum deformed state, $\eta = 4.01$ (splitting between ZFC and FC); Néel temperature $T_N$ and direction of temperature variation are indicated by arrows.

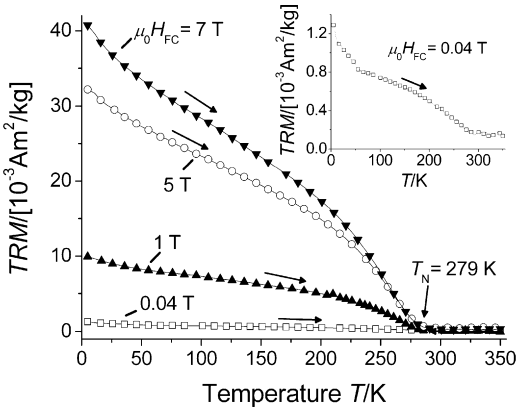


**Fig. 2.** Decay of thermoremanent magnetisation, $TRM(T)$, of the sample with $\eta = 4.01$ measured in a SQUID during warming after FC at different $H_{FC}$ from 350 K to 5 K; enlarged inset: for $\mu_0 H_{FC} = 0.04$ T. $T_N$ is indicated by an arrow. (Lines are guides to the eyes.)

$TRM(T)$ is not single valued but depends on the thermal history. Furthermore, partial TRM (PTRM) was obtained by applying the cooling field only in parts of the considered temperature range (see e.g. [35]). In particular, with respect to a reference curve of $TRM(T)$ measured after cooling the sample in an external magnetic field of $\mu_0 H_{FC} = 5$ T down to 5 K followed by heating, different states of partial thermoremanent magnetisation (PTRM1) were settled by field cooling ($\mu_0 H_{FC} = 5$ T) below $T_N$ to defined temperatures above 5 K. Then, the temperature behaviour of magnetisation was measured upon cooling and heating and is referred to as $PTRM1(T)$. According to the notation used, e.g. by Goldfarb and Patton [28] a second possible state (PTRM2) was examined by zero-field cooling to a defined temperature below $T_N$ and then applying a field $H_{FC}$ upon further cooling down to 5 K where the field is switched off again. This state and its variation with temperature is referred to as $PTRM2(T)$.

## 3. Results

### 3.1. Appearance of a thermoremanent magnetisation in the deformed state

Deformation has strong influence on the magnetic properties of the investigated fcc antiferromagnetic $Fe_{61.5}Mn_{23}Ni_7Cr_{8.5}$ alloy. By measurements of magnetisation as a function of temperature this becomes obvious by comparing measurements during warming of zero-field cooled samples with field cooling measurements. For the annealed and subsequently quenched state of a sample after hot forging, the ZFC and FC curves are identical below and above the Néel temperature $T_N$, as shown in Fig. 1. The maximum of the $\sigma(T)$-curve that marks $T_N$ is sharp. These features are the same for the annealed state at $d = 6$ mm, i.e. at zero degree of deformation, $\eta = 0$.

The $\sigma(T)$-curves of the maximum deformed state mark the distinct differences that are induced by the deformation process. Firstly, $T_N$ is lowered and the maximum in magnetisation is broadened. Secondly, a splitting between ZFC and FC magnetisation curves appears below $T_N$.

Measurements of magnetisation have been performed parallel as well as perpendicularly to the deformation axis of the samples. No differences could be found for the different major sample axes (not shown in a figure). Therefore, in particular in the figures in this study, the data of magnetisation are presented for measurements parallel to the deformation axis, only.

In order to clarify the nature of the splitting in Fig. 1, the samples were subjected to field cooling from above to below the Néel temperature and, subsequently, the magnetisation in zero field was measured during warming into the paramagnetic state. These measurements underline that the splitting arises from a thermoremanent magnetisation in the maximum deformed sample (Fig. 2) that is induced by virtue of the cooling field through $T_N$. The comparison of the splitting in Fig. 1 with the TRM after FC at $\mu_0 H_{FC} = 1$ T (Fig. 2) reveals that the magnitude is equal within experimental precision. Each cooling field induces another state with respect to the magnitude of TRM. Its stability is related to the antiferromagnetic matrix as the TRM vanishes at $T_N$.

The $\sigma(T)$-curves measured up to 9 T (VSM) after ZFC to temperatures $T$ below $T_N$ do not exhibit a significant isothermal remanence. As an example, at $T = 5$ K only very small hysteresis appears and is detectable after ZFC as well as after FC (Fig. 3). Its coercive field is as low as $\mu_0 H \approx 0.01$ T (Fig. 3). The corresponding magnetisation is already saturated at approximately $\pm 0.2$ T. However, $\sigma(T)$-curves measured after FC to below $T_N$ are shifted vertically from the origin by the amount of the induced TRM. The maximum TRM at 5 K reached after FC with $\mu_0 H_{FC} = 7$ T corresponds to about $4 \times 10^{-4} \mu_B$/atom (Bohr magneton) of a deformed afm sample.

### 3.2. Correlation of magnetisation with deformation state

The mechanical hardening during the different stages of deformation is plotted by means of indentation hardness in Fig. 4a. In a qualitative point of view this increase in hardening represents the storage and accumulation of energy during plastic deformation in form of defects, e.g. dislocations, intra-gain misorientations, small angle grain boundaries, deformation twins and at high degrees of plastic deformation also other high-angle grain boundaries.

X-ray powder diffraction studies on filings of annealed and deformed samples revealed no other phase than the face centred cubic (fcc) austenite phase, which of course cannot rule out very small amounts of $\varepsilon$-martensite.

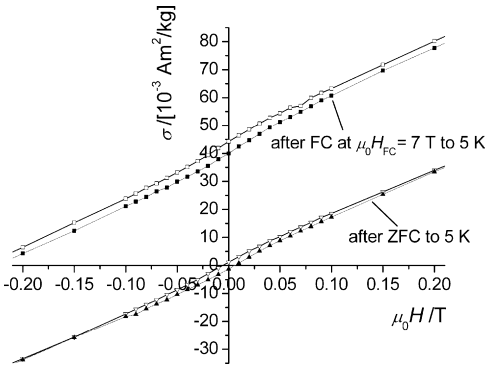


**Fig. 3.** Enlarged detail view of full isothermal magnetisation measurements, $\sigma(H)$, in the range of $\mu_0 H = \pm/\mp 7$ T of the sample with $\eta = 4.01$ at $T = 5$ K in a SQUID. Black lines and open symbols: negative field direction; grey lines, full symbols positive field direction. Triangles represent the measurement data after ZFC and squares after FC in $\mu_0 H_{FC} = 7$ T, $T = 350 \ldots 5$ K. (Lines are guides to the eyes.)

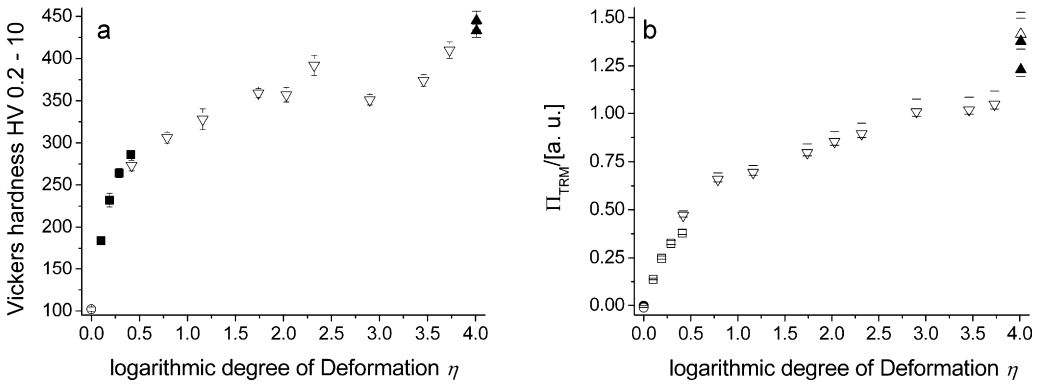


**Fig. 4.** Development of mechanical and magnetic properties with the logarithmic degree of deformation $\eta$. Circles represent the annealed state, squares tensile specimens. Downwards triangles represent wire drawn samples and upwards triangles the subsequently flat rolled samples: (a) evolution of hardening during deformation, $\eta$; (b) evolution of normalized TRM, $\Pi_{TRM}(\eta)$, as referred to the text, after FC at $\mu_0 H_{FC} = 1$ T (open symbols: measured in the VSM; filled symbols: measured in the SQUID).

The annealed samples consist of grains that are equiaxed and show homogeneous internal axis orientation. As shown by EBSD, deformation causes an increase of intra-grain misorientation by the action of dislocation slip and dislocation accumulation, as represented in Fig. 5 by the colour spread within the grain interiors. Furthermore TWIP is an active mechanism. Thin stripes of deformation twins are intersecting the grains. These have to be distinguished from annealing twins (broad bands) in the grains that formed during the preceding recrystallisation treatment.

For the characterisation of TRM evolution over the different stages of deformation a normalisation of the TRM was implemented for quantitative comparison. For all samples this evaluation was carried out on measurements of the TRM at $T = 250$ K after field cooling below $T_N$ at $\mu_0 H_{FC} = 1$ T. As shown in Fig. 1, the increase of the splitting towards lower temperatures is roughly linear in the respective range. Therefore, the normalisation is done not only with respect to the magnetisation $\sigma_{ZFC}(T = 250\,\text{K})$ in $\mu_0 H = 1$ T applied field after zero-field cooling but also necessarily to the difference $\Delta T(\eta) = T_N(\eta) - 250$ K between the actual Néel temperature of each deformed sample, $T_N(\eta)$, and the reference temperature of 250 K.

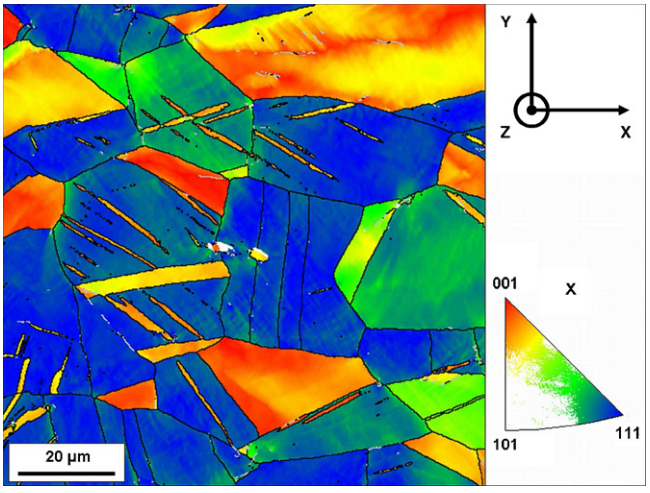


**Fig. 5.** Representation of the microstructure of the $Fe_{61.5}Mn_{23}Ni_7Cr_{8.5}$ alloy at $\eta = 0.29$ (tensile test) from an EBSD measurement (Leo 1530 FEG SEM equipped with HKL Nordlys detector, step size 0.2 µm, indexing rate 96.3%). Longitudinal section of a tensile test specimen, with the wire/tensile axis along $x$. The colour code represents the deviation from the ⟨1 1 1⟩-fiber texture orientation along $x$ as shown in the inverse pole figure on the right. Black lines represent grain boundaries with misorientations >10° and silver-grey lines with misorientations of 5°...10°.

So, the normalisation is done according to:

$$\Pi_{TRM}(\eta) = 10 \cdot \frac{\sigma_{TRM}(250\,\text{K}) \cdot T_N(\eta)}{\sigma_{ZFC}(50\,\text{K}) \cdot (T_N(\eta) - 250\,\text{K})} \quad (1)$$

This value of normalised TRM ($\mu_0 H_{FC} = 1$ T) was calculated from the measured data of all samples that were taken at different degrees of deformation and is plotted as $\Pi_{TRM}(\eta)$ in Fig. 4b. There is a striking qualitative agreement between the evolution of hardness and the magnitude of TRM in the course of deformation.

### 3.3. Characteristics of the TRM

The sample with the highest degree of deformation ($\eta = 4.01$) and consequently with the highest TRM was chosen for detailed experiments. As already implied by Fig. 2 the TRM does not saturate up to typically available fields. This non-saturating behaviour concerning the cooling field dependence of the TRM is underlined by Fig. 6. For higher magnetic fields ($H_{FC}$), the inset in logarithmic scaling shows clear correspondence in the slope of the $TRM(H_{FC})$ measured at two temperatures. However, there are slight differences in the low field regime. These differences arise from the first decrease ('tail') of the measured $TRM(T)$-curves between $T = 5$ K and $T \approx 60$ K, as observable in Fig. 2 (inset). They are related to the aforementioned small hysteresis at 5 K. Nevertheless, there is a slight transition in the slope of increasing $TRM(T)$ roughly between 0.2 and 0.6 T apparent in the logarithmic scaling (inset in Fig. 6).

For further clarification of the nature of the TRM, its dependence on the temperature range of field cooling was investigated.

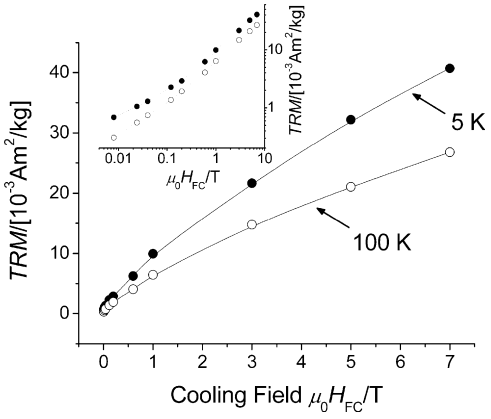


**Fig. 6.** Thermoremanent magnetisation of the sample with $\eta = 4.01$ as a function of cooling field, $TRM(H_{FC})$, after field cooling from $T = 350$ K to $T = 5$ K and $T = 100$ K respectively; inset: same plot in double-logarithmic scaling. (Lines are guides to the eyes.)

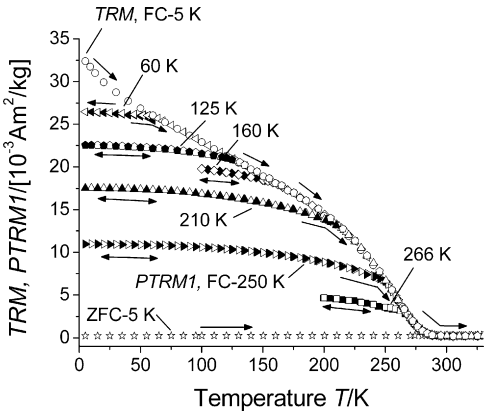


**Fig. 7.** Evolution of TRM and PTRM1 with temperature of the sample with $\eta = 4.01$ as referred to the text: base line after ZFC from above $T_N$ to $T = 5$ K (open stars); the 'master curve', $TRM(T)$, after FC at $\mu_0 H_{FC} = 5$ T from above $T_N$ to $T = 5$ K (open circles) and $PTRM1(T)$ during cooling (full symbols) and reheating (open symbols) after FC at $\mu_0 H_{FC} = 5$ T to the temperatures indicated.

For this purpose, field cooling at $\mu_0 H_{FC} = 5$ T was stopped at defined temperatures below $T_N$ and the evolution of the partial thermoremanent magnetisation ($PTRM1(T)$) in zero applied field was measured during further cooling and reheating above $T_N$. The TRM-curve measured after field cooling down to 5 K (Fig. 7) is equivalent to the 5 T-curve in Fig. 2. With respect to the $PTRM1(T)$-curves it represents a 'master curve' in several aspects. The TRM-values measured after the field had been switched off at the temperature indicated in Fig. 7 fall together with this 'master curve'. All $PTRM1(T)$-curves lie below the 'master curve' and follow the same path during cooling and subsequent heating until they reach the temperature at which the cooling field $H_{FC}$ was ramped down during FC. At this point every thermoremanent state, which was settled by the different FC conditions reaches the 'master curve' and turns into it until all TRM vanishes at the Néel temperature.

In the case of partial thermoremanent magnetisation measurements, where the sample was zero-field cooled from above $T_N$ to a temperature below $T_N$ and further field cooled at $\mu_0 H_{FC} = 5$ T down to 5 K (PTRM2), the evolution of thermoremanent magnetisation with temperature (Fig. 8a) is different from that of the $PTRM1(T)$ in Fig. 7. During heating in zero field the TRM vanishes at the temperatures, where the magnetic field was applied for further FC down to $T = 5$ K. The remanent magnetisation reached after FC to 5 K from the temperatures, $T = 125$ K and $T = 160$ K, is equal within experimental accuracy and the curvature of their $PTRM2(T)$ is positive over the whole temperature range. In contrast the $PTRM2(T)$-curves for FC from $T = 210$ K and $T = 250$ K show a transition from positive to negative curvature. Their inflection point is roughly between $T = 150 \ldots 170$ K.

The thermoremanent magnetisation induced after PTRM2 field cooling is also very stable. Only the small additional magnetisation mentioned before is visible during the $\sigma(H)$-measurement between $\mu_0 H = \mp 6.5$ T (not shown here). The overall $\sigma(H)$-curve remains vertically shifted and symmetric with respect to the $\sigma$-axis. Consequently, a stable thermoremanent magnetisation of comparable magnitude can be reached by different field cooling procedures, e.g. FC at 5 T from above $T_N$ to $T = 250$ K and further cooling in zero field (Fig. 7), FC at 1 T from above $T_N$ to $T = 5$ K (Fig. 2) and ZFC down to $T = 160$ K or 125 K followed by FC at 5 T to 5 K (Fig. 8a). However, the temperature dependences of remanent magnetisation in the case of $PTRM1(T)$, $TRM(T)$ and $PTRM2(T)$ are distinctly different.

Remarkably, the $PTRM1(T)$ and $PTRM2(T)$ curves are additive and sum up to be equal to the 'master curve' within experimental accuracy as shown in Fig. 8b.

## 4. Discussion

### 4.1. Origin of TRM

The presented experimental data of Figs. 1 and 4 reveal that the appearing TRM has its origin in the deformation of the investigated alloy, i.e. deformation induced defects are responsible for the observed changes of the primary properties of the afm as well as its remanence after field cooling (Figs. 2, 7 and 8). Vacancies as isolated zero dimensional faults can be ruled out as major sources of TRM for two reasons. Firstly, a high concentration of vacancies should also be present in the quenched state after annealing, where no TRM is observed (Fig. 1). Secondly, vacancies are not the defects governing plastic deformation and hardening and, consequently, they cannot be the source of the observed TRM (Fig. 4). Thermally induced vacancies in metallic alloys have concentrations in the order of $10^{-4}$ (vacancies/total lattice sites) and therefore they are very diluted and the random distribution of uncompensated moments with respect to the sublattices will statistically cancel out over the sample volume. These isolated moments are strongly coupled to the afm and cannot be polarised in magnetic fields used in this study (Fig. 1).

Effects of exchange bias (EB) resulting in remanent magnetisation have also been ascribed to spin canting in the afm due to exchange coupling of the afm to ferromagnetic entities [36]. An

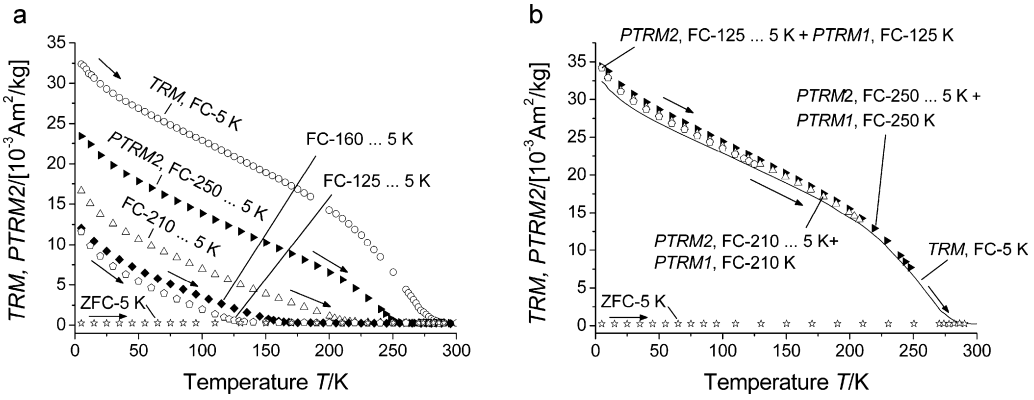


**Fig. 8.** Evolution of TRM and PTRM2 with increasing temperature of the sample with $\eta = 4.01$ as referred to the text. Base line after ZFC from above $T_N$ to $T = 5$ K (open stars): (a) the 'master curve', $TRM(T)$, after FC at $\mu_0 H_{FC} = 5$ T from above $T_N$ to $T = 5$ K (open circles) and $PTRM2(T)$ after ZFC from above $T_N$ and FC at $\mu_0 H_{FC} = 5$ T from the temperatures indicated to $T = 5$ K. (b) $PTRM2(T) + PTRM1(T)$ (data taken from (a) and Fig. 7) showing the additivity of PTRM1 and PTRM2 to the full $TRM(T)$ (for better visibility drawn as a line).

implementation of this concept to the afm alloy under investigation would mean that the non-collinear afm spin structure is modified by its exchange coupling to the uncompensated spins induced by deformation. Such secondary effects are expected to be small and will not be considered further.

In fact, deformation and hardening of this $Fe_{61.5}Mn_{23}Ni_7Cr_{8.5}$ alloy is governed by two modes (Fig. 5): 'conventional' deformation by formation, slip and accumulation of dislocations as well as deformation twinning (TWIP). Both modes are likely to disturb the long range antiferromagnetic order, i.e. TWIP by continuous fragmentation into differently oriented and smaller grains and dislocations by the local reduction of crystal symmetry and their stress fields. Therefore, long range afm order is heavily affected and intrigued by the structural disorder, that has to be incorporated into the afm state below $T_N$. The consequences as deduced from the experiments (Fig. 1) are an inhomogenisation and weakening of the afm. The former is marked by a broad maximum implying a spectrum of Néel temperatures within the deformed afm sample. The latter can be deduced from the decrease of magnetic ordering temperature and an increase in overall susceptibility with respect to the annealed sample (Fig. 1). In isothermal $\sigma(H)$-measurements of the deformed sample susceptibility is also higher (not shown). A decrease of $T_N$ due to disorder is known from diluted afm systems [37].

As a consequence of the extraordinary stability of the TRM it can be concluded that the uncompensated moments that are produced by the defects are strongly exchange coupled to the surrounding antiferromagnet. From magnetic measurements sensing the entire response of the sample it is hard to determine the kind of defects that produce the TRM with endmost certainty. However, it is possible to give reasoning about the most probable defects as described in Section 1. There is surely a contribution of high-angle grain boundaries (HAGB) as they are likely to nest uncompensated moments. But they cannot be expected to yield the major contribution. Also HAGB are already present in the annealed state where no TRM is observed (Figs. 1 and 4b). Furthermore, HAGB formed during deformation are only expected to be produced at a high degree of deformation, where according to Fig. 4 most of the TRM is already present. Twin boundaries produced by TWIP (Fig. 5) are in fact a special case of fully coherent HAGB ($\Sigma 3$ in the coincidence site lattice treatment). The discrimination whether these are responsible for the appearance of TRM is more difficult. For the samples taken from tensile specimens after testing twinning is most prominent between $\eta = 0.19, \ldots, 0.41$ (only $\eta = 0.29$ exemplarily shown, Fig. 5). The evolution of TRM qualitatively lacks behind the evolution of work hardening and the strong increase of the latter is mainly due to the dynamic grain refinement by deformation twinning. Hence, dislocations and small-angle grain boundaries (SAGB) are more likely to be the main origin of TRM in the deformed alloy. Furthermore, as the twin–matrix orientation relationship is defined by a 60° rotation about a common ⟨1 1 1⟩-axis and as its interface is fully coherent at the twin habit plane, this special planar defect might not produce a high amount of uncompensated moments with respect to the special afm spin structure [6,9] of this type of alloy.

An estimate further promotes the idea of dislocations being responsible for the TRM. Taking the maximum obtained moment of about $4 \times 10^{-4} \mu_B$/atom (Section 3.1), this gives about $4.6 \times 10^{16}$ uncompensated moments with a reasonable value of $1\mu_B$ within the sample. By assuming only the atoms inside the dislocation lines to carry these moments this gives an estimated dislocation line length that, divided by the sample volume, would yield to a dislocation density of, $\rho_V \approx 8.8 \times 10^{11}\,\mathrm{cm}^{-2}$. This is a reasonable value for a highly deformed metallic alloy. Furthermore, formation of additional HAGB due to deformation would be expected at a later stage of deformation and, hence, qualitatively produce a $\Pi_{TRM}(\eta)$-curve different from that shown in Fig. 4b. However, from these considerations a contribution of HAGB cannot be ruled out completely.

Different observations indicate that a spectrum of defects is responsible for the TRM. Firstly, the TRM magnitude does not saturate from the lowest up to the highest applied cooling fields (Figs. 2 and 6). Secondly, a variety of sample conditions can be settled depending on the field cooling procedure and temperature as presented in Figs. 7 and 8. This also corresponds to the broad distribution of the afm ordering temperature mentioned before. The integral measurements of the samples magnetisation do not allow a quantification of this defect spectrum. It can be thought of as a statistical distribution of isolated dislocations, ranging between the two terminal configurations of complete screw and edge character as well as stacking faults and partial dislocations. Any kind of defect clusters thereof arranged as entangled or 'forest' dislocations and SAGB together with possibly minor contributions of HAGB might be part of this distribution. Consequently, defects of different size and/or dimensionality have to be expected and, regardless of the exact structure of the defects, a change of slopes of the cooling field dependence as shown in the inset of Fig. 6 would not be surprising.

### 4.2. Low temperature hysteresis

The small hysteresis observed in $\sigma(H)$-measurements at 5 K as described in Section 3.1 (see Fig. 3) and Section 3.3 can be considered to be overlaid with the stable TRM and produces a low-temperature 'tail' in the *TRM*($T$)- and FC $\sigma(T)$-curves of the deformed sample ($\eta = 4.01$) which can be seen in Figs. 1, 2 and 7. By reversing this magnetisation after a PTRM2 field cooling procedure from $T = 160$ K down to $T = 5$ K at $\mu_0 H_{FC} = 5$T and subsequent warming during $\sigma(T)$-measurement in zero field, a discrimination of the superimposed magnetisation from the stable TRM is possible. For this purpose the *PTRM*2($T$)-curve with afore reversed superimposed magnetisation at $T = 5$ K is subtracted from the corresponding *PTRM*2($T$)-curve shown in Fig. 8. As a result, its $\sigma(T)$-behaviour could be determined to be spin-glass-like with a freezing temperature of $T_f \approx 60$ K (not shown here).

Similar types of low temperature glass-like magnetic states are known from the Fe–Mn–system [2,38] and are attributed to spin-frustration at the coherent interface between the austenitic afm matrix and submicron-sized needles of hexagonal afm $\varepsilon$-FeMn martensite [39]. The Néel temperature of this $\varepsilon$-FeMn martensite is about $T_N \approx 210$ K [4].

Only in some of the $\sigma(T)$-measurements done at finite applied field, overlaid maxima in the respective temperature range were found. However, those were not reproducible for all measurements in contrast to the TRM, which are not affected. So, if the formation (and decomposition upon heating) of small $\varepsilon$-martensite fractions is assumed, this process will occur in a stochastic manner with respect to the applied experimental procedures. These difficulties in interpretation arise from the metastability of the austenite phase, reminding that the equilibrium state of these alloys is inhomogeneous [2].

As the 'tail' magnetisation and its hysteresis are only superimposed and as irrespective of some indications on minor effects of $\varepsilon$-martensite, the TRM were stable and reproducible, this 'tail' magnetisation has not to be accounted for with respect to the origins of the highly stable TRM.

### 4.3. Temperature dependence of the stable TRM

A major consequence of the presented experimental data is that no isothermal remanence can be created, i.e. (within the limits of fields used in this study) a remanent magnetisation is obtained solely by application of a magnetic field during cooling below $T_N$

(Figs. 7 and 8). As the stable TRM does not saturate with the magnitude of applied field, $H_{FC}$ (Fig. 6), and because the *TRM*(*T*)-curve still shows a considerable slope towards the lowest temperatures (also without the 'tail' magnetisation, Fig. 2) the 'master curve', as defined in Fig. 7, does not reflect the temperature dependence of TRM in general. It only represents the *TRM*(*T*) for this special case of cooling the sample to the lowest experimental temperature, whereas the *PTRM*1(*T*)-curves reveal the thermomagnetic behaviour of the presumed magnetised defects, which is independent of field-cooling effects taking place at lower temperatures. In this sense the 'master curve' represents the state of the sample that is settled at a given cooling field from above $T_N$ and the temperature at which it is switched off, because all *PTRM*1(*T*)-curves converge with the 'master curve' at the respective temperature in Fig. 7. The form of the 'master curve' is quite different from the *TRM*(*T*)-curve that Takano et al. [30,31] measured for stable TRM in afm multilayers, where the temperature behaviour of TRM reflects that of the staggered magnetisation of the afm CoO/MgO multilayers. By comparing these results with the *TRM*(*T*) of the deformed $Fe_{61.5}Mn_{23}Ni_7Cr_{8.5}$ alloy, a correspondence between its bulk afm staggered magnetisation and its *TRM*(*T*) is not apparent and might only be assumed for the temperature range right below $T_N$. Antiferromagnetic γ-Fe–Mn alloys show nearly Brillouin-type behaviour in their staggered magnetisation as known from neutron diffraction experiments [5,40]. Therefore, a completely negative curvature has to be expected with nearly horizontal course towards zero temperature, which is even in a qualitative comparison only true down to about $T = 160$ K for the 'master curve' in Fig. 7. Otherwise, the *PTRM*1(*T*)-curves represent the 'real' temperature dependence of the remanent magnetisation in so far as they well fit to Brillouin functions with *T* normalised to $T_N = 294$ K of the annealed sample until they fall together with the 'master curve' (not shown). Nevertheless, typical features of the investigated TRM due to uncompensated moments are similar to the ones observed by Takano et al. [30], e.g. the qualitatively similar cooling field dependence of TRM as in Fig. 6 [31]. Further, O'Grady et al. [33] describe a cooling field dependence of the ordering of uncompensated spins at the afm/fm interface in EB systems, which causes an increase of the remanent EB field for increasing cooling field. This dependence also does not saturate up to the maximum applied field of 2 T which is far above the saturation field of the fm layer. This has been explained by processes of thermal activation in the EB system. However this scenario is not yet really understood.

Not only the fact that the deformed sample cannot be switched in the thermoremanent state by laboratory fields but also that the *PTRM*1(*T*)-curves follow exactly the same path during cooling and heating (Fig. 7), clearly reveals the high stability of TRM in the deformed sample. Only strong exchange coupling to the afm matrix can be considered to deliver such a stabilisation [24]. The vanishing of TRM and PTRM1 right at the Néel temperature supports this interpretation (Figs. 2 and 7). Vertical shifts of $\sigma(H)$-curves after field cooling as observed for the deformed alloy are clear evidence for a special case of exchange anisotropy. Meiklejohn [41] underlined that, if small ferromagnetic clusters are rigidly coupled to the antiferromagnet, i.e. they cannot be switched by laboratory fields, their magnetisation curve can also be considered to be shifted along the magnetisation axis. Upwards shifts of minor loops of magnetisation-vs.-magnetic field curves have been reported also on afm multilayer systems [31] and have been attributed to strongly coupled uncompensated surface spins [30–32]. Schmid et al. [29] however interpreted upwards shifts of minor loops in EB systems to a large extent to defects within the volume of the afm layers.

As discussed in Section 4.1, dislocations and accumulations of dislocations are identified to be the most likely defects to carry remanently magnetised uncompensated moments in the deformed alloy. Their size and also an assumed volume of disturbed afm order around them easily fulfil the criterion of a small entity with respect to the afm matrix. The description of uncompensated moments in an antiferromagnet by Néel [17] was referred to afm nanoparticles with uncompensated moments at the surface that are afm and superparamagnetic (spp) at the same time. The term superparamagnetic had been introduced by Bean [42] to describe small ferromagnetic particles that, above a so called blocking temperature, $T_B$, behave similar to paramagnetic particles, due to thermal fluctuations. Of course, in materials such as considered in this study, lots of other, even more complicated local magnetic configurations at the aforementioned defects are possible. Néel further predicted that a dislocation in a bulk antiferromagnet should behave in the same way as an uncompensated sublattice plane of an afm nanoparticle [43]. However, the coupling of a dislocation in a bulk antiferromagnet may be considered to be larger, because a half plane of any dislocation is surrounded by the parent antiferromagnet and not coupled to just a single half space of afm ordered material – as it is the case for an uncompensated surface layer. It has been shown by Skumryev et al. [44] for Co/CoO core shell nanoparticles that exchange anisotropy not only results in a shift of the hysteresis loops in the magnetisation-field-plane but also causes an increase of the blocking temperature of superparamagnetic objects. Thus, the TRM of the defects might be addressed in terms of superparamagnetic uncompensated spins that are thermally stabilized by exchange coupling to the bulk afm. During FC the uncompensated moments are magnetised by the external field and, due to their exchange coupling to the afm, they create the net bias field to which they are blocked during further cooling, because they influence the spin order of the surrounding afm volume near $T_N$. This interpretation is consistent with the reported blocking [28] and stabilisation [44] of superparamagnets by the assistance of an imposed afm EB field in rather different material systems. A further consequence of such a blocking mechanism would be an accommodated domain state of the afm as the magnetised defect clusters would force the orientation of the neighbouring afm spin orientation. Takano [31] also considered that the thermal demagnetisation of TRM arising from uncompensated spins in CoO/MgO multilayer systems is suggestive of a blocking mechanism.

As presented so far, the reasoning to explain the observed effects, can be considered as most probable but it only holds true for the two *PTRM*1(*T*)-curves, where the magnetic field was applied from above $T_N$ to temperatures *T* below but near the broad susceptibility maximum as observed in Fig. 1, i.e. about $T_N > T > 160$ K. There has to be a second process involved that remanently magnetises further defects, because a further significant increase of *TRM*(*T*) in Fig. 7 below $T \approx 160$ K cannot be explained after afm ordering in the deformed alloy is completely established. This also becomes clear by the astonishing behaviour of the *PTRM*2(*T*) (Fig. 8). Support to invoke a secondary or modified process for further TRM formation is given by a change of slope in the respective temperature range in the $\sigma(T)$-curves of the deformed sample (Fig. 1) as well as by the inflection of the *PTRM2*(*T*)-curves in Fig. 8a. It is considered that, until the inflection temperature, TRM is primarily formed according to the blocking process as described so far, which includes the consequence, that the disordered afm samples show a continuous ordering process until this inflection temperature is reached. The subsequent increase of TRM with different slope in Fig. 7 and the formation of thermal remanence as given by the *PTRM*2(*T*)-curves in Fig. 8a is more difficult to understand. Similar phenomena have been reported for EB systems containing afm grains of different size and, consequently, different energy barriers for thermal blocking [33]. Certainly thermally activated setting of fractions of the highly deformed afm has also to be considered as a mechanism to explain the increase of remanence values far below $T_N$ in Figs. 2, 7 and 8a as well as the non-saturation of *TRM*($H_{FC}$) in Fig. 6.

For materials with a microstructure as complex as that of the material investigated here, theoretical description of their magnetic behaviour is hard to find in literature. A rather well investigated system is the diluted Ising antiferromagnet in an external field (usually abbreviated DAFF, [45]). A DAFF develops a multi-domain state when field cooled below its Néel temperature [46]. A domain state in diluted antiferromagnets was also deduced from experiments and the domain walls are believed to reduce their energy by incorporating the defects [47]. Comparable effects are expected also for other types of distorted antiferromagnets and, in particular, afm domains based on defects are considered as common features in the afm part in typical EB systems consisting of a ferromagnetic subsystem coupled to an antiferromagnet [48]. According to these findings, the afm state of the deformed sample at $T \approx 160$ K might be addressed as a multi-domain state, where some domain orientations are already fixed by exchange anisotropy with the already blocked spp moments. Domain walls are attached to the remaining spp defects that have not blocked at the respective temperature yet. As the anisotropy field in the afm domain wall can be considered to be weak compared to that in the afm domain volume, these defects can still be polarised by the external field and continuously block upon further cooling. Since, in this scenario, only the domain walls are still magnetically polarisable into a thermoremanent contribution it seems reasonable that the final PTRM2 reached by FC from 160 . . . 5 K and 125 . . . 5 K are approximately equal (Fig. 8a).

Within the framework of this partially intuitive interpretation the additivity of the $PTRM1(T)$ and $PTRM2(T)$ to the full $TRM(T)$-curve is a striking support as presented in Fig. 8b. From rock magnetism it is known that blocking of individual superparamagnetic entities of different size happens independently from each other in the ideal case of TRM [35], so that the corresponding $PTRM(T)$ are additive to sum up to the full $TRM(T)$. Even though not independent from the surrounding afm volume, the independence of the individual blocking events can be clearly seen.

## 5. Conclusions

The distinct changes of the magnetic state that occur in a metallic, austenitic and antiferromagnetic alloy due to the impact of deformation are reported. These are at first, a decrease of the Néel temperature and considerable differences in the character of the magnetisation-vs.-temperature behaviour with rising degree of deformation, that are attributed to an inhomogenisation of the afm state. Further, a splitting between the ZFC $\sigma(T)$-curves and the $\sigma(T)$ measured during as well as after FC appears for the deformed samples. This splitting has been shown to be connected to a small but very stable TRM that can be induced by field cooling the deformed samples.

Uncompensated moments at the deformation induced defect sites that are strongly exchange coupled to the bulk antiferromagnet are discussed to be the origin of the TRM. This magnetisation cannot be switched by laboratory fields up to 9 T as observed, e.g. as a vertical shift of $\sigma(H)$-curves. The magnitude of TRM does not saturate with applied cooling field and shows a considerable increase down to the lowest temperatures achieved during field cooling. It was further proven that the amount of TRM scales with the degree of deformation that is present in the respective samples. This scaling is correlated with the hardening behaviour of the investigated alloy.

Given the responsibility of deformation induced defects to account for the TRM, it is discussed that a variety of defects can be involved in the observed effects. Dislocations are however the most probable defect sites to deliver clusters of uncompensated moments and represent themselves a broad distribution in character and size due to the expected dislocation substructures that evolve with increasing degree of deformation.

The interpretation of the temperature dependence of the thermoremanent magnetisation in zero field after different field cooling procedures addresses the defects to behave like superparamagnets that are blocked by the assistance of an afm exchange bias field during field cooling.

Even though speculative, two processes are identified to take place. Firstly, the defects with a high effective blocking temperature impose an anisotropy on the neighbouring afm spins to which they consecutively block during further cooling. This process evolves over a considerable temperature interval which is identified to be the ordering interval of the antiferromagnet, whose structural order is heavily disturbed by deformation. Secondly, a smaller fraction of the assumed defect distribution is not blocked until the end of the afm ordering process. These defects are considered to be the preferred sites for afm domain walls, as the deformed alloy can be expected to build up a domain state similar to a diluted antiferromagnet. As the afm exchange interaction is weakened within the domain walls the domain structure will be modified during field cooling down to the lowest temperatures and, therefore, will further increase the TRM. This process might likewise be considered as a thermally activated change of the afm state in the smaller and disturbed fractions of the deformed alloy together with blocking of the associated uncompensated moments in the cooling field.

It can be concluded that internal defect structures – especially dislocations – within a deformed antiferromagnetic alloy are responsible for stable TRM and distinct but complex changes of the overall afm behaviour. Disorder in antiferromagnets can, therefore, be a source of small (about $4 \times 10^{-4} \mu_B$/atom) but very stable (hard) magnetisation. Assuming that the observed effects are not only linked to the special non-collinear spin structure of austenitic afm FeMn-base alloys, the importance of defects in afm materials has to be underlined. As dislocations (and other defects) are also not unlikely to occur in thin film materials this work might give new complementary insights for the evaluation of the magnetic state of afm layers in exchange bias systems.

## Acknowledgements

The authors thank M. Frey, D. Seifert, T. Wolf, M. Gründlich, S. Yin, C. Rodig, H. Klauss, V. Neu and A. Voss for experimental support.

## References

[1] H. Schumann, Metallographie, 12th ed., Verlag für Grundstoffindustrie, VEB Deutscher, 1987.
[2] E.F. Wassermann, in: K. Buschow, E. Wohlfarth (Eds.), Ferromagnetic Materials, vol. 5, North-Holland, Amsterdam, 1990, pp. 240–322 (Chapter 3).
[3] H.H. Ettwig, W. Pepperhoff, Phys. Status Solidi A 23 (1) (1974) 105–111.
[4] W. Pepperhoff, M. Acet, Constitution and Magnetism of Iron and its Alloys, 1st ed., Springer-Verlag, Berlin/Heidelberg, 2001.
[5] Y. Endoh, Y. Ishikawa, J. Phys. Soc. Jpn. 30 (6) (1971) 1614–1627.
[6] H. Umebayashi, Y. Ishikawa, J. Phys. Soc. Jpn. 21 (7) (1966) 1281–1294.
[7] S.J. Kennedy, T.J. Hicks, J. Phys. F: Met. Phys. 17 (7) (1987) 1599–1604.
[8] S. Kennedy, T. Hicks, J. Magn. Magn. Mater. 81 (1–2) (1989) 56–62.
[9] J. Kouvel, J. Kasper, J. Phys. Chem. Solids 24 (4) (1963) 529–536.
[10] M. Shiga, J. Phys. Soc. Jpn. 22 (2) (1967) 539–546.
[11] S. Allain, J.P. Chateau, O. Bouaziz, S. Migot, N. Guelton, Mater. Sci. Eng. A 387 (2004) 158–162.
[12] O. Grassel, L. Kruger, G. Frommeyer, L.W. Meyer, Int. J. Plast. 16 (10–11) (2000) 1391–1409.
[13] L. Rémy, A. Pineau, Mater. Sci. Eng. 28 (1) (1977) 99–107.
[14] L. Rémy, Acta Metall. 25 (2) (1977) 173–179.
[15] I. Karaman, H. Sehitoglu, K. Gall, Y.I. Chumlyakov, H.J. Maier, Acta Mater. 48 (6) (2000) 1345–1359.
[16] J.W. Christian, S. Mahajan, Prog. Mater. Sci. 39 (1–2) (1995) 1–157.
[17] L. Néel, C. R. Hebd. Acad. Sci. 252 (1961) 4075–4080.
[18] G. Toulouse, Commun. Phys. (London) 2 (1977) 115–119.
[19] A.J. Mydosh, Spin Glasses: An Experimental Introduction, Taylor & Francis, London, 1993.

[20] C. Lacroix, B. Canals, M.D. Núñez-Regueiro, B. Coqblin, J. Arispe, Physica B 230–232 (1997) 529–534.
[21] L. Néel, C. R. Hebd. Acad. Sci. 253 (1961) 9–12.
[22] W.J. Schuele, V.D. Deetscreek, J. Appl. Phys. 33 (3) (1962) 1136–1137.
[23] W.H. Meiklejohn, C.P. Bean, Phys. Rev. 102 (5) (1956) 1413–1414.
[24] W.H. Meiklejohn, C.P. Bean, Phys. Rev. 105 (3) (1957) 904–913.
[25] J.S. Kouvel, C.D.J. Graham, I.S. Jacobs, J. Phys. Radium 20 (2) (1959) 198–202.
[26] J.S. Kouvel, C.D.J. Graham, J. Phys. Chem. Solids 11 (1959) 220–225.
[27] J.S. Kouvel, J. Phys. Chem. Solids 16 (1960) 152–157.
[28] R.B. Goldfarb, C. Patton, Phys. Rev. B 24 (3) (1981) 1360–1373.
[29] I. Schmid, P. Kappenberger, O. Hellwig, M.J. Carey, E.E. Fullerton, H.J. Hug, Europhys. Lett. 81 (1) (2008) 17001.
[30] K. Takano, R.H. Kodama, A.E. Berkowitz, W. Cao, G. Thomas, Phys. Rev. Lett. 79 (6) (1997) 1130–1133.
[31] K. Takano, Exchange anisotropy in thin film bilayers of nickel cobalt monoxide and various ferromagnetic materials, Ph.D. thesis, University of California, San Diego (1998).
[32] A.E. Berkowitz, K. Takano, J. Magn. Magn. Mater. 200 (1999) 552–570.
[33] K. O'Grady, L.E. Fernandez-Outon, G. Vallejo-Fernandez, J. Magn. Magn. Mater. 322 (2010) 883–899.
[34] L. Néel, Ann. Géophys. 5 (1949) 99–136.
[35] D.J. Dunlop, J. Appl. Phys. 93 (10) (2003) 8236–8240.
[36] N.C. Koon, Phys. Rev. Lett. 78 (25) (1997) 4865–4868.
[37] D. Belanger, F. Borsa, A. King, V. Jaccarino, J. Magn. Magn. Mater. 15–18 (Part 2) (1980) 807–808.
[38] W. Stamm, Strukturelle und magnetische Inhomogenitäten in kubisch flächenzentrierten 3d-Invarlegierungen, Ph.D. thesis, Universität-GH-Duisburg (1988).
[39] E. Gartstein, A. Rabinkin, Acta Metall. 27 (6) (1979) 1053–1064.
[40] Y. Ishikawa, Y. Endoh, J. Phys. Soc. Jpn. 23 (2) (1967) 206–213.
[41] W.H. Meiklejohn, J. Appl. Phys. 33 (3) (1962) 1328–1335.
[42] C.P. Bean, J. Appl. Phys. 26 (11) (1955) 1381–1383.
[43] L. Néel, C. R. Hebd. Acad. Sci. 253 (1961) 203–208.
[44] V. Skumryev, S. Stoyanov, Y. Zhang, G. Hadjipanayis, D. Givord, J. Nogués, Nature 423 (2003) 850–853.
[45] S. Fishman, A. Aharony, J. Phys. C: Solid State 12 (18) (1979) L729–733.
[46] A. Glaser, A.C. Jones, P.M. Duxbury, Phys. Rev. B 71 (2005) 174423.
[47] W.C. Barber, F. Ye, D.P. Belanger, J.A. Fernandez-Baca, Phys. Rev. B 69 (2004) 024409.
[48] P. Miltényi, M. Gierlings, J. Keller, B. Beschoten, G. Güntherodt, U. Nowak, K.D. Usadel, Phys. Rev. Lett. 84 (18) (2000) 4224–4227.